Electronic Supplementary Material (ESI) for Nanoscale.

Supporting Information

for

Competing oxidation mechanisms in Cu nanoparticles and their plasmonic signatures

Sara Nilsson[1,†], *Monia Runge Nielsen*[2], *Joachim Fritzsche*[1], *Christoph Langhammer**[,1] *and*
*Shima Kadkhodazadeh***[,2, †]

[1] Department of Physics, Chalmers University of Technology, 412 96 Göteborg, Sweden

[2] DTU Nanolab, Technical University of Denmark, Fysikvej, 2800 Kgs Lyngby, Denmark

[†]equal contribution

*clangham@chalmers.se; **shka@dtu.dk

Content

S1. *In situ* ADF STEM – EELS: 4D data acquisition and visualization

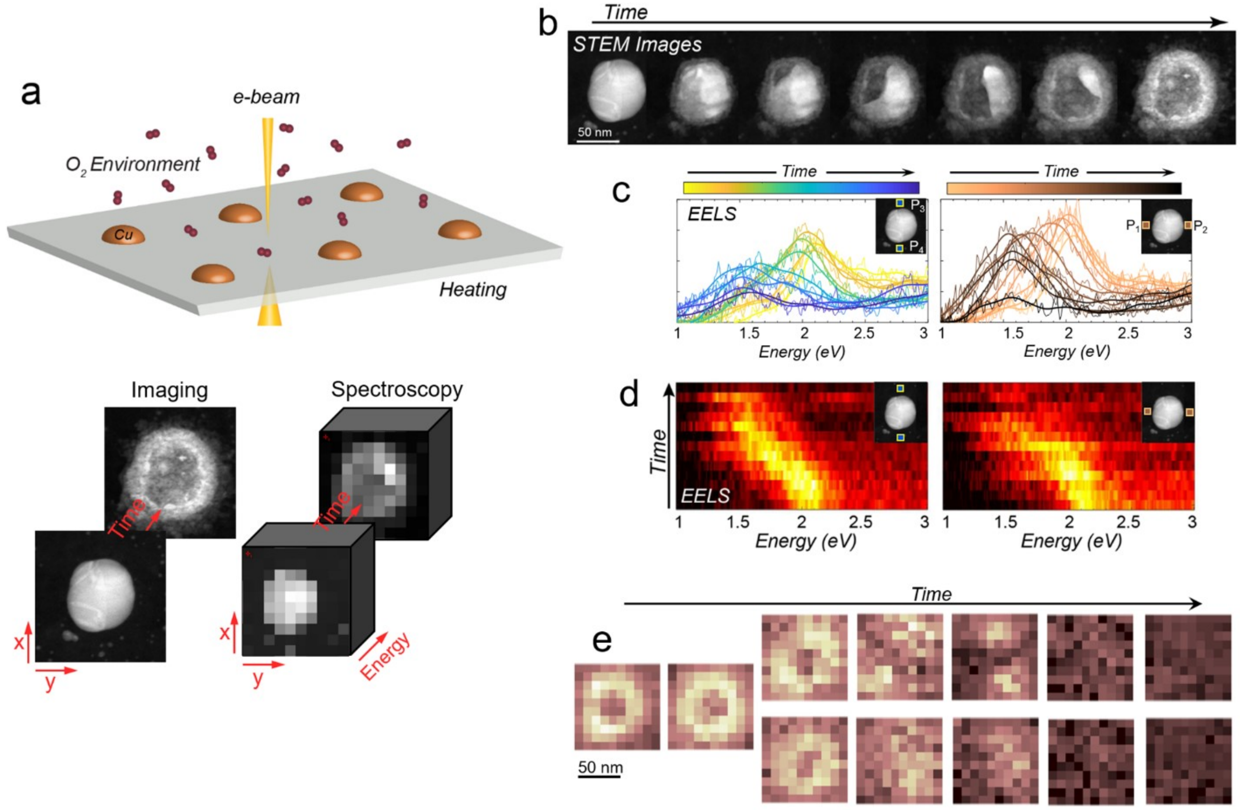

Figure S1: The concept of in situ STEM and EELS. *(a) A schematic of the environmental STEM – EELS approach used for the in situ STEM imaging and EELS during Cu nanoparticle oxidation at elevated temperatures. ADF STEM images (~0.3 nm resolution) and EELS spectrum images (10 x 10 pixels) were recorded concurrently at regular time intervals during the oxidation. (b) Some of the recorded images revealing the morphological evolution of the particle during oxidation, which then can be correlated with the EELS data. The 4D EELS data (dimensions x, y, energy and time) visualised as (c) a series of EEL spectra recorded through time from the positions around the particle marked with squares in the inset STEM image. The presented spectra are the sum of the two EEL spectra acquired from the marked positions with matching colors (spectra to the left are sum of spectra from P_3 and P_4 and spectra to the right are sum of spectra from P_1 and P_2). (d) Intensity maps of the spectra associated with the same pixel position through time, and (e) a series of 2D maps of the intensity of the EEL signal at energies of interest (e.g. LSPR peak energy) through time.*

S2. Oxidation experiments

S2.1. ADF STEM images of additional particles oxidized at 50 °C

In **Figure S2.1**, there are images of additional particles oxidized at 50 °C during the same experiment as the 50 °C particle in Figure 1 in the main text. None of the particles exhibit a nanoscale Kirkendall void at this temperature, and the average oxide thickness after 90 minutes of O_2 exposure in all particles was 5.5 ± 0.7 nm.

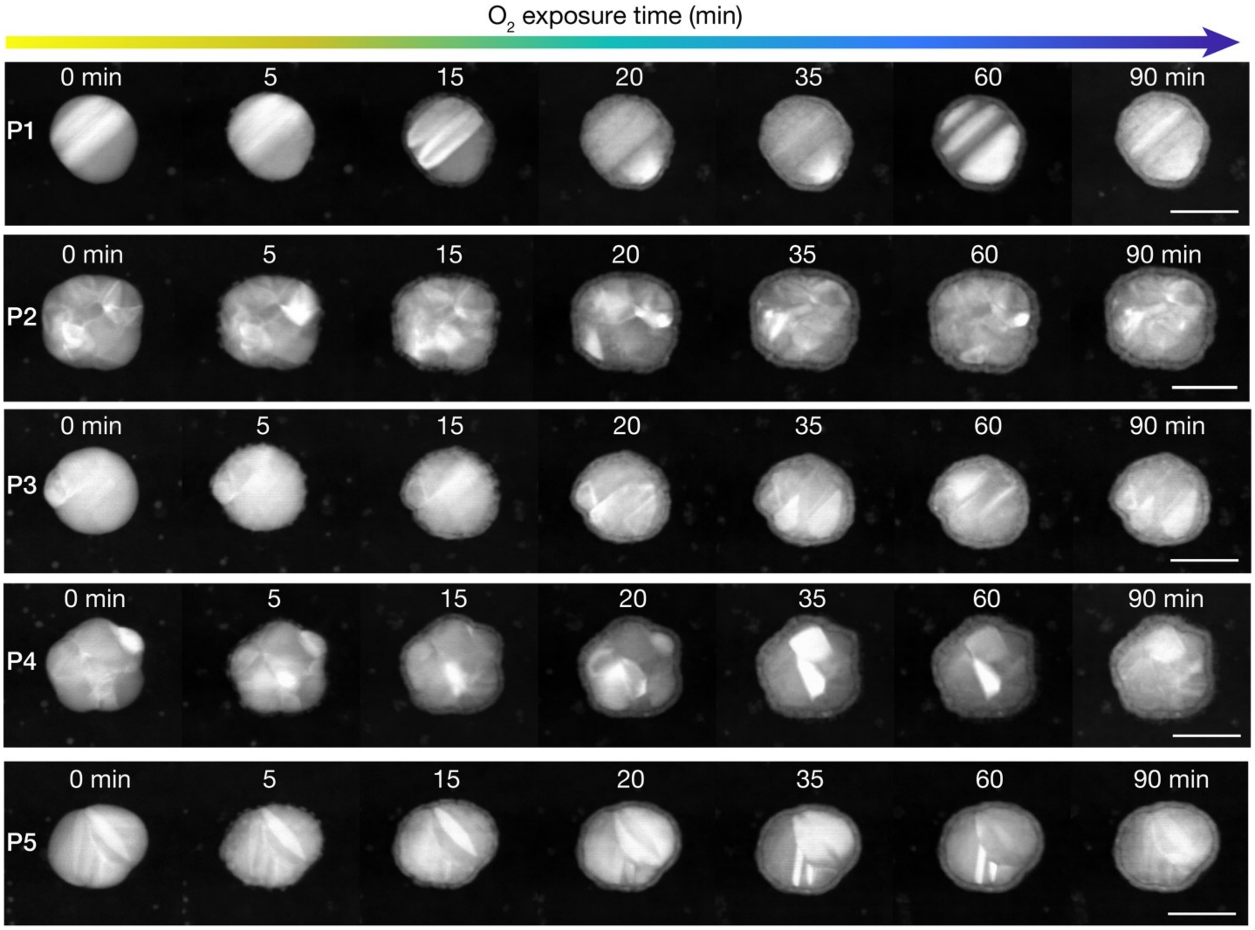

Figure S2.1: Self-limiting oxide growth in particles oxidized at 50 °C. *Selected STEM images of additional particles oxidized at 50 °C, under the same conditions as the particle presented in Fig. 1 in the main text. The accumulated O_2 exposure time is indicated for each frame. All scale bars are 50 nm.*

S2.2. ADF STEM images of additional particles oxidized at 100 – 200 °C

Additional examples of the evolution of the NK void in particles at temperatures 100, 150 and 200 °C after the formation of a single void at the metal-oxide interface (**Fig. S2.2**), which then expands with a close to linear front until approximately half of the metallic core from void nucleation has been oxidized ($\delta = 60 \pm 10$ %). The void expansion then switches to an angular growth mode for the rest of the oxidation process.

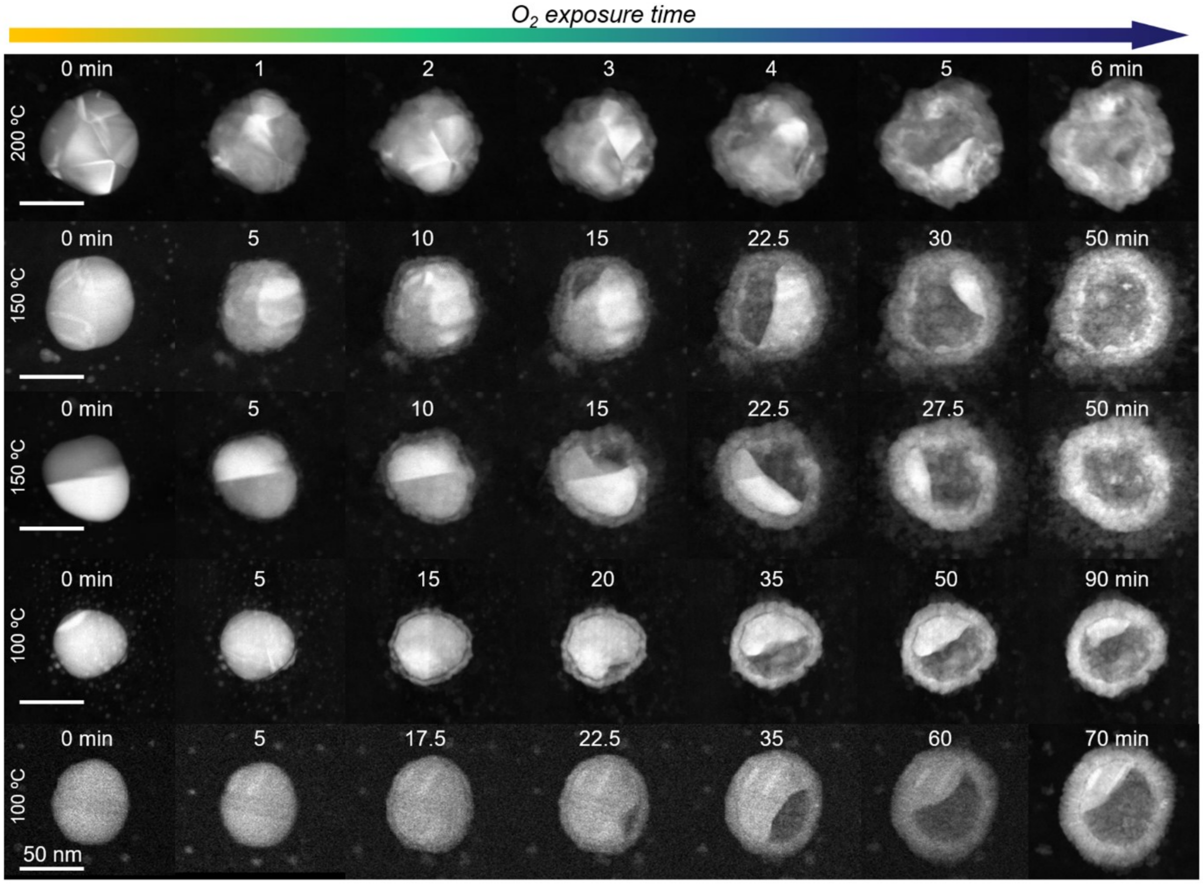

Figure S2.2: Additional particles exhibiting the linear to angular void front scenario. *ADF STEM image sequences of additional Cu particles oxidized at 100, 150 and 200 °C (the temperature is indicated on the left side) with a void expansion in the fashion described in the text, where the NK void growth front expands linearly initially, followed by an angular expansion after approximately 60 % volume of the particle has been oxidized.*

S2.3. ADF STEM images of the NK void evolution in larger particles

ADF STEM images of particles at 100, 150 and 200 °C, where more than one NK void is formed during oxidation (**Fig. S2.3)**. This is typically observed in larger and more polycrystalline particles.

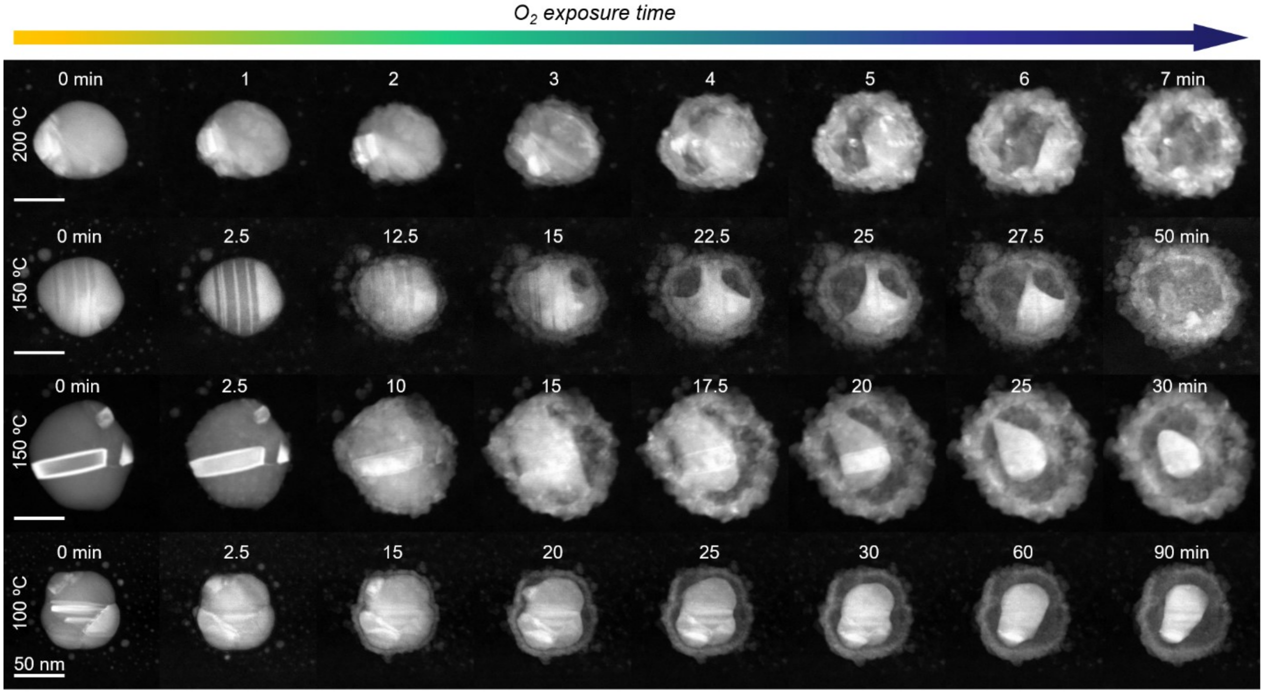

Figure S2.3: Oxidation path of larger particles. *STEM images of particles oxidized at 100, 150 and 200 °C, showing the formation of multiple NK voids.*

S2.4. Core-loss EELS chemical analysis of oxidized particles

Core-loss EELS was used to determine the chemical state of the different parts of oxidized nanoparticles. **Figure S2.4a** shows Cu and O composition maps (top row) and a map of their relative compositions for the inner and outer shells of a hollow oxide nanoparticle (bottom row; oxidized at 200 °C). The maps were composed from the EELS signal containing the O K-edge and Cu $L_{2,3}$-edge. The energy dispersion per channel for the acquisitions was 0.5 eV (energy range acquired spanning from 300 – 1300 eV) and the acquisition time per pixel 0.4 s. **Figure S2.4b-c** show the energy-loss near-edge structure of O K- and Cu $L_{2,3}$-edges recorded from the inner and outer oxide shells of the particle and plotted together with standard signals from Cu, Cu_2O, Cu_4O_3 and CuO, revealing that both shells are mostly composed of Cu_2O and the outer shell also contains Cu_4O_3.

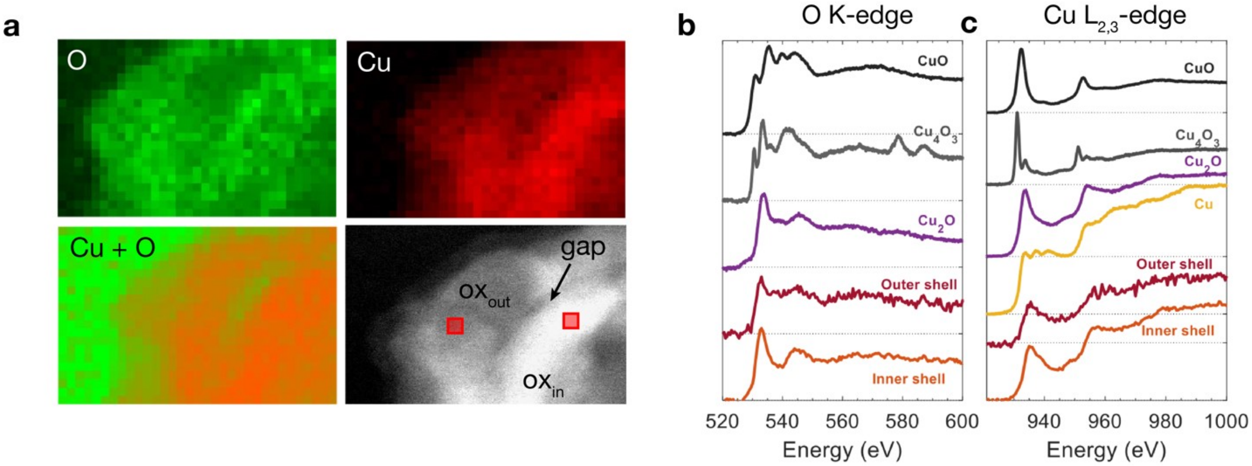

Figure S2.4: Core-loss EELS of the inner and outer oxide shells. *(a) Intensity maps of the EELS O K-edge and Cu $L_{2,3}$ -edge signals from the area marked by a rectangle in the particle oxidized at 200 °C in the STEM image. At the position of the gap shell, we note that the Cu atom density is significantly lower compared to the inner and outer oxide shells. Example (b) O K-edge and (c) Cu $L_{2,3}$ -edge spectra from the inner (orange) and outer (red) oxide shells (positions marked by red squares in (a)) together with standard O and Cu core-loss spectra of CuO[1], Cu_4O_3[2] and Cu_2O[1], demonstrating that both oxide shells are mostly composed of Cu_2O, with traces of CuO and Cu_4O_3 in the outer shell.*

S2.5. *In situ* EELS of LSPR at 50 °C

In **Figure S2.5**, there are three additional Cu particles to the one in Figure 2 in the main text simultaneously oxidized at 50 °C for an accumulated O_2 exposure time of 90 minutes. The same observations are made for these particles; (i) the two excited polarizations follow each other throughout the experiment, (ii) initially the change is small or a slight blue-shift is observed during the initial oxide island formation, and (iii) a red-shift and intensity increase which coincides with the formation of the homogenous oxide layer (marked by the dashed line).

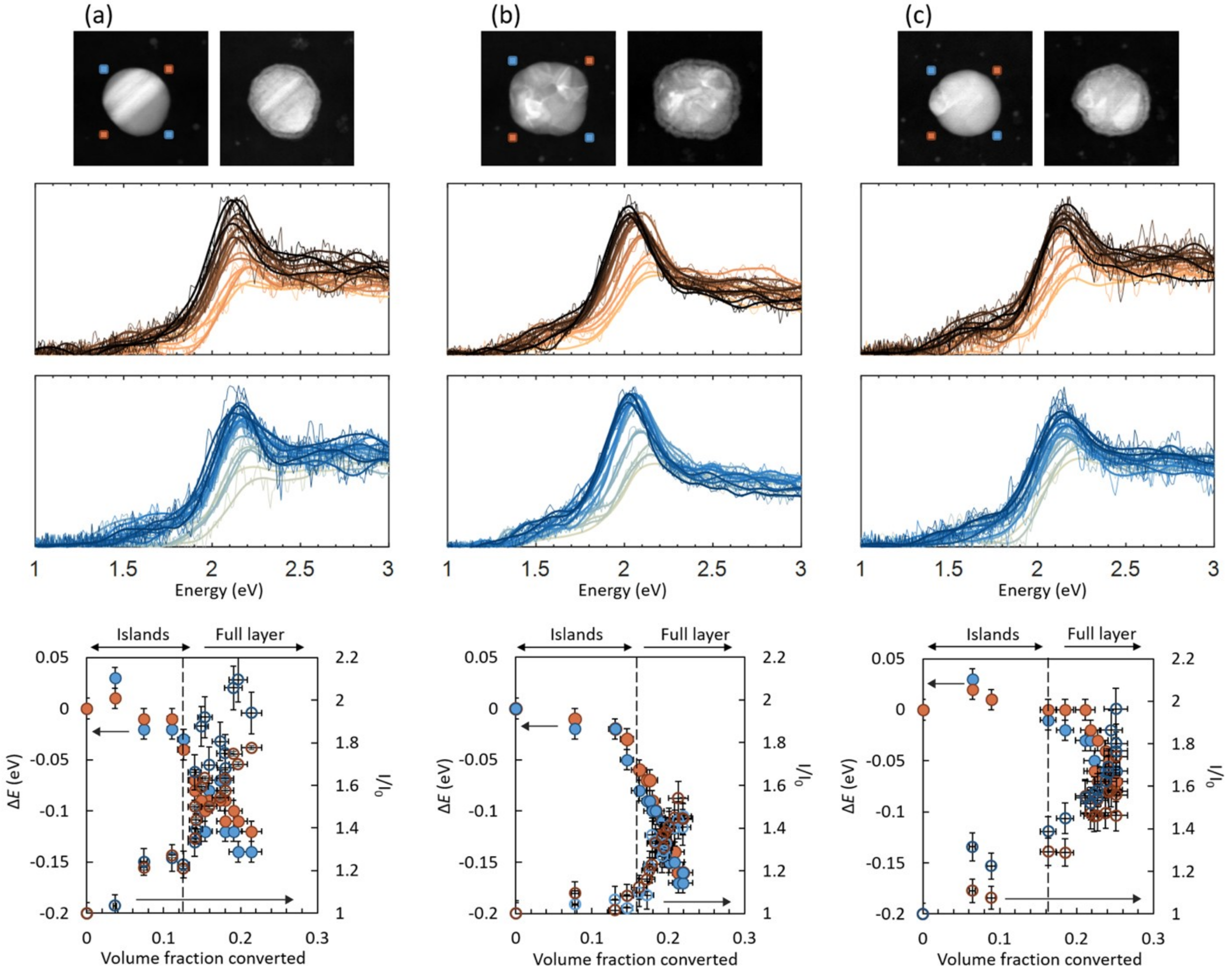

Figure S2.5: EELS of additional particles oxidized at 50 °C. *(a, b, c) Additional examples of particles oxidized at 50 °C simultaneously with the particle in Figure 2 in the main text. From the top, the particles imaged before and after 90 minutes of O_2 exposure with the beam positions marked for acquiring the EEL spectra (brown and blue). In the bottom panels, the LSPR peak energy shift (filled circles) and the relative intensity change (empty circles) vs. the fraction of oxidized metal, δ, is plotted for each of the frames.*

S2.6. Kirkendall void nucleation and growth

The volume oxidation fraction at which we observe the nucleation of the NK void does not show a clear dependence on size in the particle radius range 25 - 50 nm (**Fig. S2.6**). However, we observe a slightly higher oxidation fraction threshold for void growth nucleation at higher temperature. The mean of all 4 samples at 100 – 200 °C is $\bar{\delta}_{void} = 23 \pm 8$ %. However, if we focus only on the 100 and 150 °C measurements, we find a lower $\bar{\delta}_{void}(100, 150\ °C) = 20 \pm 4$ % and at 200 °C, $\bar{\delta}_{void}(200\ °C) = 33 \pm 8$ %. Studying the onset of NK void growth as a function of sizes, we should remember that we have only studied a handful of particles at each temperature, and only two size groups (35 and 50 nm) at the same temperature, 150 °C. With this in mind, these averages does not have statistical significance. The observed higher $\bar{\delta}_{void}$ at higher temperature can be a consequence of the higher oxidation rate and consequently δ increases more between frames.

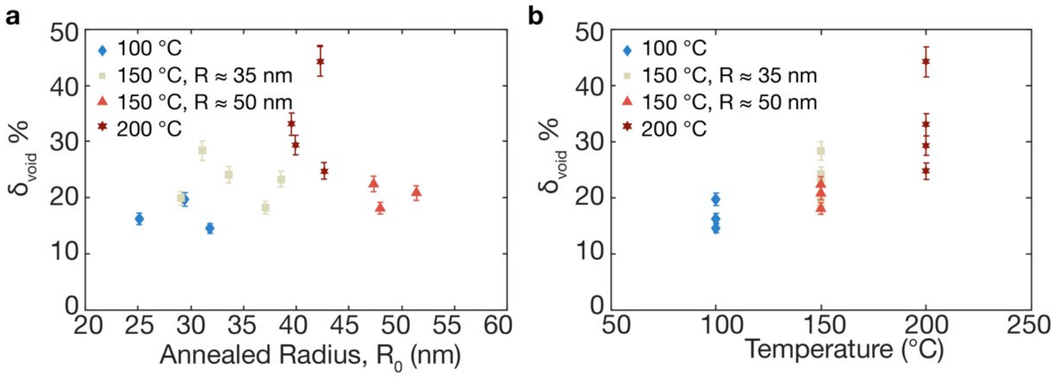

Figure S2.6: ***Void nucleation.*** *(a) The volume oxidation fraction at NK void nucleation, δ_{void}, vs. annealed particle radii and (b) δ_{void} vs. temperature. Note, there is no clear trend in the studied range of particle radii 25 - 50 nm. However, there is a trend to higher δ_{void} at higher temperature. The error bars indicate the uncertainty in the image segmentation.*

S2.7. *In situ* EELS of LSPR at 150 °C and 200 °C

The LSPR evolution of Cu particles oxidized at 150 °C and 200 °C is depicted in **Figure S2.7**. The particles follow a similar morphological evolution as the particle oxidized at 100 °C in Figure 3 in the main text.

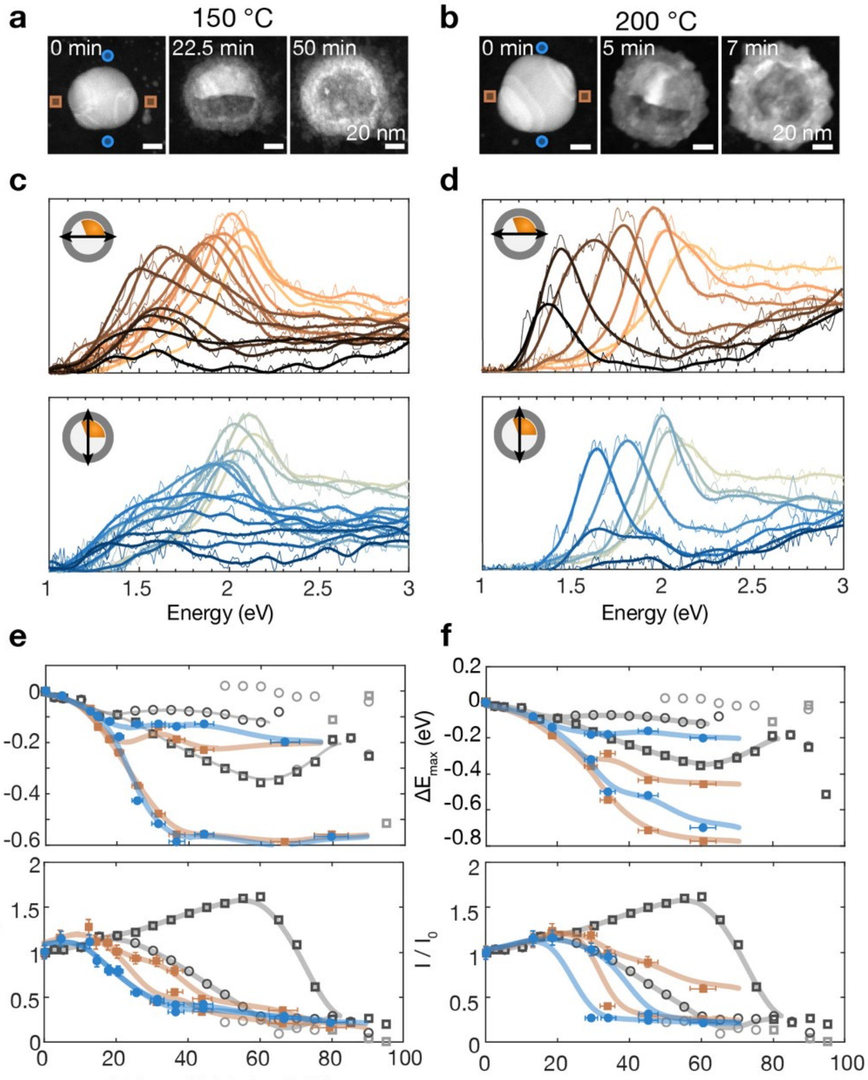

Figure S2.7: EELS of particles oxidized at 150 and 200 °C*. ADF STEM images of Cu particles oxidized at (a) 150 °C and (b) 200 °C with a void expansion according to the process described in the main text. (c, d) The LSPR modes probed by EELS in the positions marked in the ADF STEM images. (e, f) The peak energy and intensity of the LSPR modes together with the FDTD simulated peak energies and intensities calculated according to the geometries in described in Section S4.*

S3. Geometrical metal-oxide interface area considerations

Upon its growth, the shape of the Kirkendall void dictates the metal-oxide interfacial area and thus the corresponding surface energy. To understand the systems' observed preference to change void growth mode from linear to angular once more than 50 % of the metal core has been consumed, we calculate the metal-oxide interfacial area for two simplified cases: (i) a linear void front moving all the way across the Cu core (red line), and (ii) an angularly expanding void front (pink line in **Fig. S3**). The observed scenario corresponds to the void front that minimizes the interfacial energy at each percentage of consumed metal, which results in a linearly expanding void front for 0 – 50 % of consumed metal core, and an angularly expanding void front for 50 – 100 %. The area of the metal-oxide interface in the linear void front case is calculated by a spherical cap geometry, and for the angular void front it is calculated by the partial surface area of a hemisphere. This analysis reveals that the straight void front expanding toward the particle center is at first minimizing the metal-oxide interface. However, after reaching the center, it is more energetically favorable to expand the void in an angular fashion in terms of minimizing the interfacial energy, in agreement with the experimentally predominantly observed scenario (cf. Fig. 1 and Fig. 3 in the main text).

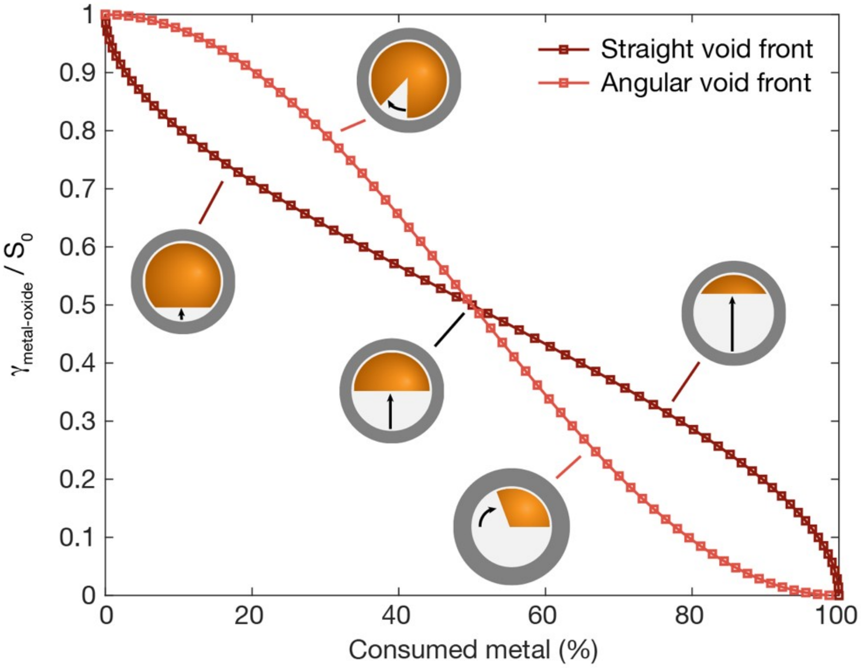

Figure S3: Minimizing the metal-oxide interface. *Calculation of the metal-oxide interface, $\gamma_{metal\text{-}oxide}$, ratio to initial metal surface area, S_0. We compare a straight and angularly expanding void as function of the consumed metal core. The results demonstrate that a straight void-metal front* *minimizes the metal-oxide interface from 0 – 50 % of consumed metal core, but from 50 – 100 % it is the angularly expanding void that minimizes the metal-oxide interface.*

S4. Electrodynamic simulations

Finite-difference time-domain (FDTD) electrodynamic simulations (ANSYS Lumerical) were employed in order to interpret the EELS LSPR data. The oxidation phases were simulated using a number of different geometries based on the STEM images. Based on the STEM images we identified the following phases: i) oxide islands nucleation, ii) growth of a homogeneous oxide shell, iii) void nucleation and iv) void expansion starting out linearly and at $\delta = 60 \pm 10$ %, when the void has consumed approximately 50 % of the metal core left at the void nucleation, it turns to expand angularly.

S4.1. The island nucleation phase: 0 – 10 % oxidation fraction

During oxidation from 0 – 10 %, the EELS LSPR is not shifting or shows a slight blue-shift of 0.1 - 0.2 eV at 50 °C. This oxidation stage, which from the STEM images is identified as the oxide island nucleation phase, was simulated by FDTD using the parameters summarized in **Table S4.1.** The models at $\delta = 5$ and 10 % are visualized in **Figure S4.1**. The total volume of oxide in the islands is calculated to match the amount of Cu converted to oxide at each oxidation fraction, and the Cu core radius, *R,* is implemented to shrink accordingly. Furthermore, the model includes edge rounding of the base of the hemisphere with a radius of 5 nm equivalent to the models used at higher volume oxidation fractions, which for simplicity is omitted in the schematics in **Figure S4.1**. The mesh overlay used in all three simulations had a size of 0.25 nm (0.2 nm was also tested and gave a similar result within the estimated error margin). In the model, the positions of the oxide islands on the hemisphere are random, and the error in volume due to overlapping islands is considered small and has therefore been neglected.

Table S4.1: *The parameters used in the simulation of the island nucleation phase.*

Volume Oxidation δ (%)	Number of islands	Island radius R_{island} (nm)	Cu core radius R (nm)
2.5	230	2	34.7
5	230	2.5	34.4
10	270	3	33.8

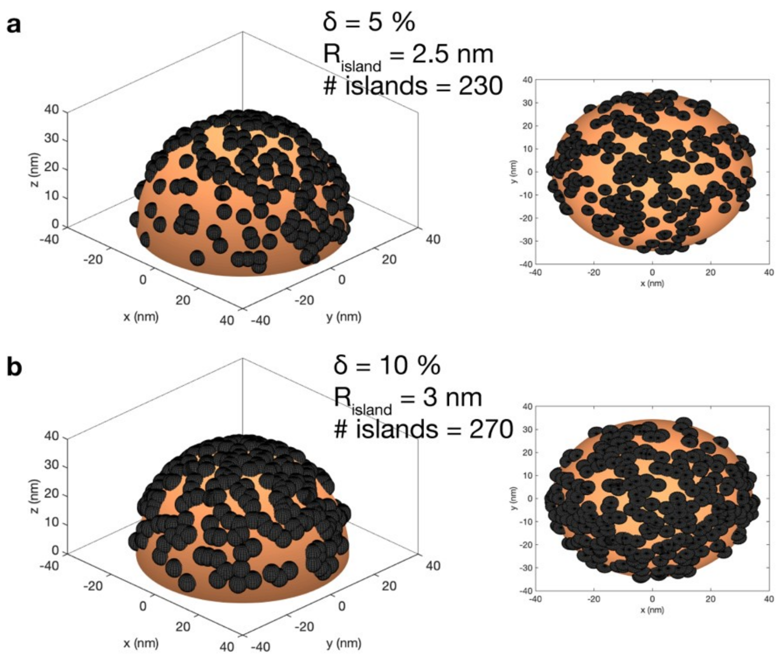

Figure S4.1: Schematic examples of random oxide island distributions. *A hemispherical Cu nanoparticle (pink) employed to model the oxide island (gray) nucleation at (a)* $\delta = 5\ \%$ *with 230 oxide islands of radius* $R_{island} = 2.5$ *nm and (b)* $\delta = 10\ \%$ *with 270 oxide lands of radius* $R_{island} = 3$ *nm. The values of* R_{island} *are based on the STEM images and the number of islands are calculated in order to reach the right oxide volume.*

Additionally, two extreme cases of oxide island distribution were tested. As depicted in **Figure S4.2,** in the extreme case all islands are located on one half of the hemisphere and the applied electrodynamic field is either polarized parallel or perpendicular to the axis that divides the oxide island dense side from the empty side. The idea of this model was to test whether the distribution of the oxide islands could have an effect on the LSPR response excited in different directions. Interestingly, however, the difference in the response was minimal, which leads to the conclusion that no LSPR effect from the island distribution is to be expected. The peak shift observed for the extreme island distribution onto only one side was slightly smaller compared to the case when islands randomly cover the whole hemisphere. However, the difference is small enough to be an effect of the likely larger error due to overlapping islands, which leads to a larger oxide volume loss in the asymmetric model.

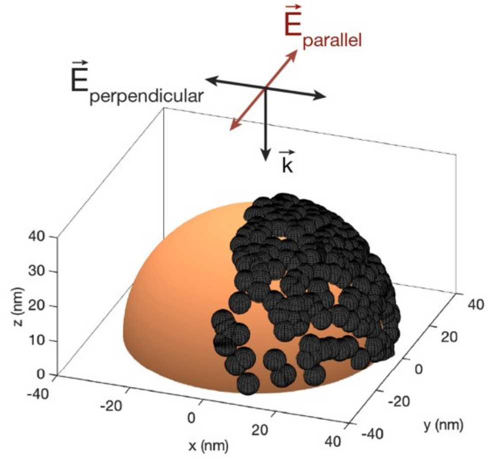

Figure S4.2: Asymmetric oxide island distribution. *Schematics of the extreme case where all oxide islands are nucleated on one half of the particle hemisphere. The arrows indicate the orientation of the parallel and perpendicularly applied electromagnetic field.*

For comparison, we also simulated a linearly increasing homogeneous oxide shell growth from the start of oxidation, together with a shrinking metal radius, *R*, to account for the consumption of metal. This is compared with LSPR absorption peak shift and the relative intensity change of the simulation of the island models in **Figure S4.3.**

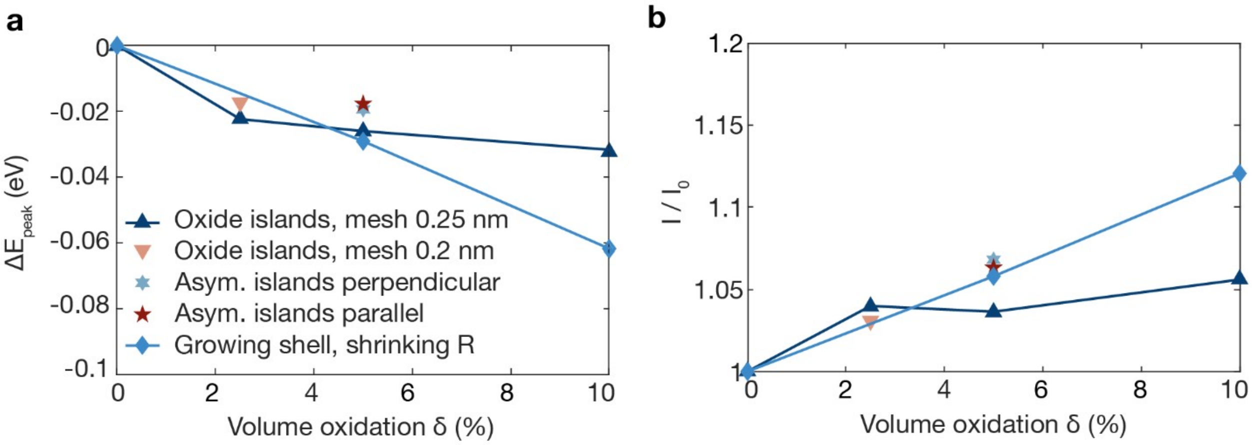

Figure S4.3: FDTD simulations of δ = 0 – 10 %. *(a) The LSPR peak energy shift and (b) relative peak intensity of the island models; the random oxide island distribution with 0.25 nm (◘) and 0.2 nm mesh overlay (❑), asymmetric island distribution (islands on one side) with the applied polarization parallel (➚) or perpendicular (⬇), compared with the homogeneously growing oxide shell and shrinking core radius R (🕘).*

We observe that the island model after $\delta = 10$ % gives a smaller red-shift compared to the growing homogenous oxide shell. For reference, a homogeneous oxide shell with the same thickness as the island radius, R_{island}, but diluted with vacuum by Maxwell-Garnett mixing to mimic a porous oxide, was tested and gave rise to a linear red-shift with respect to δ that was slightly larger than the one plotted in **Figure 4.3** for the homogeneous oxide growth. The fact that the simulated homogeneous shell does not reproduce the initially slower red-shift in the experimental data, which the oxide island model does reproduce, indicates that it is the non-homogeneous distribution of the oxide along the Cu-surface that gives the initial slower red-shift.

The second observation made for $\delta < 10$ % was that several of the particles imaged during oxidation at 50 °C display a blue-shift in the EELS LSPR response. We speculate that there could be two potential reasons for the observed blue-shift: i) the Cu core shrinks due to that Cu atoms from the surface are converted to oxide, which leads to a decrease in the metallic volume (**Fig. S4.4**), and ii) changes in the surface electronic structure of Cu induced by oxygen adsorption and dissociation[3] since the induced d-band shift leads to a smaller overlap with the LSPR and thus lower LSPR damping, as discussed in the main text.

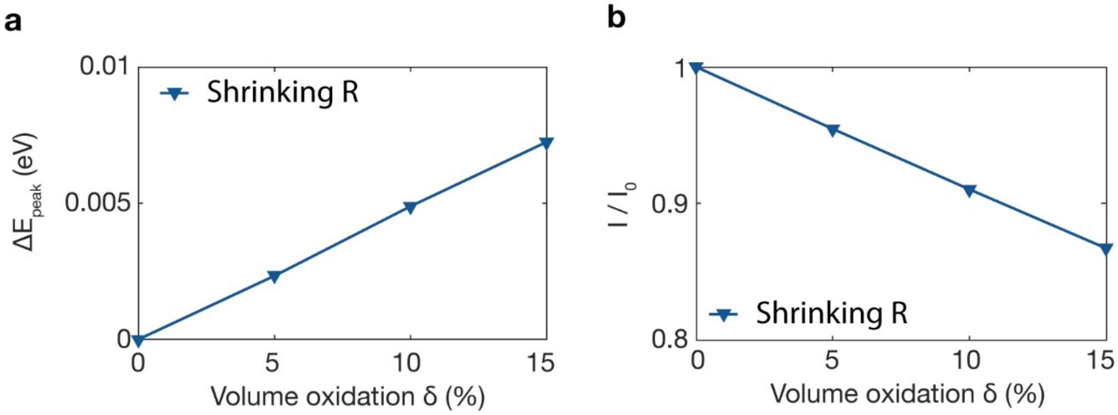

Figure S4.4: The LSPR of the shrinking metal core. *(a) The LSPR peak energy shift and (b) relative peak intensity of the simulated LSPR response of solely the Cu core shrinking upon 0 – 15 % volume oxidation.*

The blue-shift is observed already for the first EELS data point at around $\delta = 5$ % and the simulated blue-shift due to a volume decrease (**Fig. S4.4**) at this δ is only about 10 % of the experimentally observed blue-shift. It is therefore unlikely that the blue-shift is due to volume decrease alone and that it to the larger extent is the consequence of decreased LSPR damping due to the d-band shift induced by oxygen adsorption.

S4.2. Homogenous oxide shell growth before NK: 15 – 20 % oxidation fraction

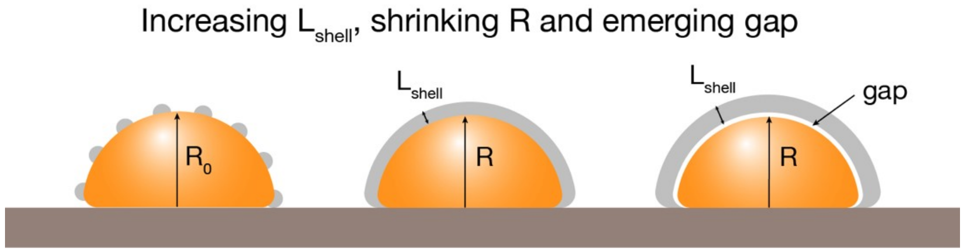

Figure S4.5: Homogeneous oxide shell growth. *When the complete oxide layer is formed and continues to grow homogeneously, the Cu atoms traversing the oxide shell give rise to a layer of Cu vacancies at the metal-oxide interface, i.e. form a gap layer.*

Following the island nucleation phase, we observed a phase of homogenous growth with the oxide shell covering the full particle. In the majority of particles oxidized at 50 °C, this transition occurred after 10 minutes of oxidation and an average of δ = 15 %. Therefore, from 15 % the oxidation was modelled as a complete oxide shell. During this phase, the gap between the oxide and the Cu core emerged, due to that Cu vacancies accumulated at the metal-oxide interface when Cu atoms traversed the oxide shell. To model this scenario, we simulated that the gap emerging after δ = 15 %, with parameters according to **Table S4.2** and a mesh overlay of 0.25 nm.

Table S4.2: *The parameters used to simulate the transition to a homogenous shell and the emergence of the gap layer.*

Oxidation fraction δ (%)	**Oxide thickness L_{Shell} (nm)**	**Gap (nm)**	**Cu core radius R (nm)**
15	3	0	33.2
20	3.9	0.7	33.2
22	4.0	1.0	33.2

The combined simulation models, which describe the oxidation process until the nucleation of the NK void, are summarized in **Figure S4.6** and the likeliest LSPR evolution based on the ADF STEM images includes; i) the island nucleation phase, ii) the homogenous oxide growth and iii) the emergence of the vacancy gap. The LSPR path corresponding to this scenario is marked in **Figure S4.6** by the gray shaded area including an error margin of ± 10 % (for the peak shift 10 % of the δ = 20 % shift is used). The peak shift and relative intensity change of this so called "likeliest scenario" is used in Fig. 2 and 3 in the main text.

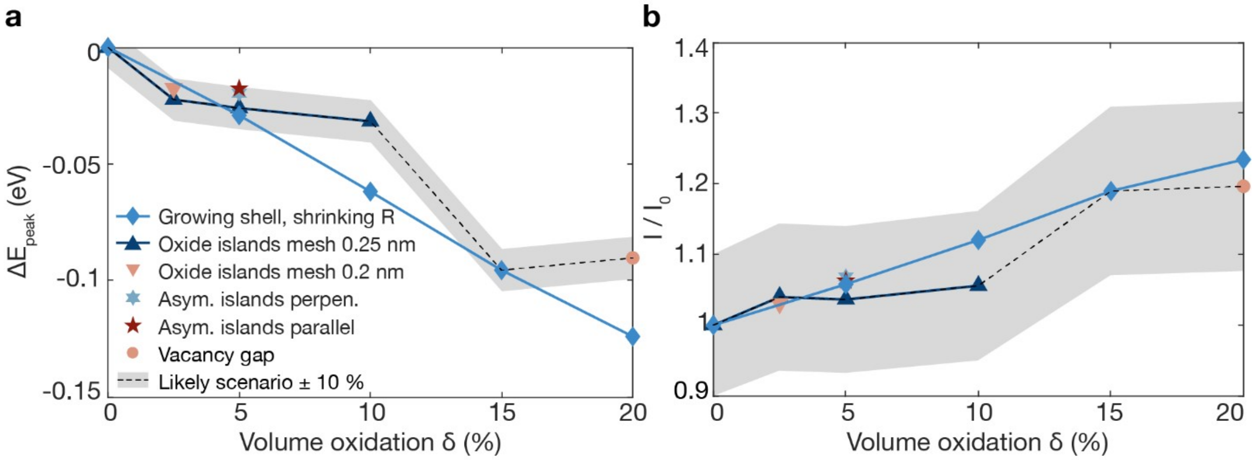

Figure S4.6: The simulated LSPR evolution for δ = 0 – 20 %. *(a) The LSPR peak energy shifts and (b) the relative peak intensities of all the FDTD simulations during the initial oxidation phase for the homogeneously growing oxide shell and shrinking radius R of the Cu core (🕘), the random oxide island distribution with mesh overlay of 0.25 nm (□), and with mesh overlay of 0.2 nm (❑), the asymmetric island distribution with the polarization parallel (➚) or perpendicular (➘) to the side with oxide islands, and the homogeneous oxide shell with the vacancy gap shell emerging at the interface between oxide and metal core after δ = 15 % (●). The gray area marks ± 10 % of the response of the model geometries which are closest to the STEM images and therefore the likeliest alternative.*

S4.3. NK void formation and expansion: 25 – 100 % oxidation fraction

To model the NK void growth with FDTD we combined three separate geometries to emulate the three phases of oxidation after the oxide island nucleation (**Fig. S4.7**). The overall Cu nanoparticle geometry is a hemisphere of R_0 = 35 nm, with 5 nm edge rounding. The geometrical parameters used at each of the simulated 5 % volume oxidation steps are calculated based on the void nucleation from δ = 22 % and are summarized in **Table S4.3**. The mesh overlay was 0.25 nm for δ= 25 – 60 % and 0.5 nm for δ= 65 – 95 %, as well as for the initial fully metallic Cu hemisphere. Constant values were used for the radius (R = 33.2 nm), the vacancy gap (1 nm) and the point of void nucleation (δ = 22 %). The FDTD model is a simplification of the complex process we observe experimentally, and we have therefore not included the inner oxide shell. However, the effect of adding the inner oxide shell is discussed in Section S4.4.

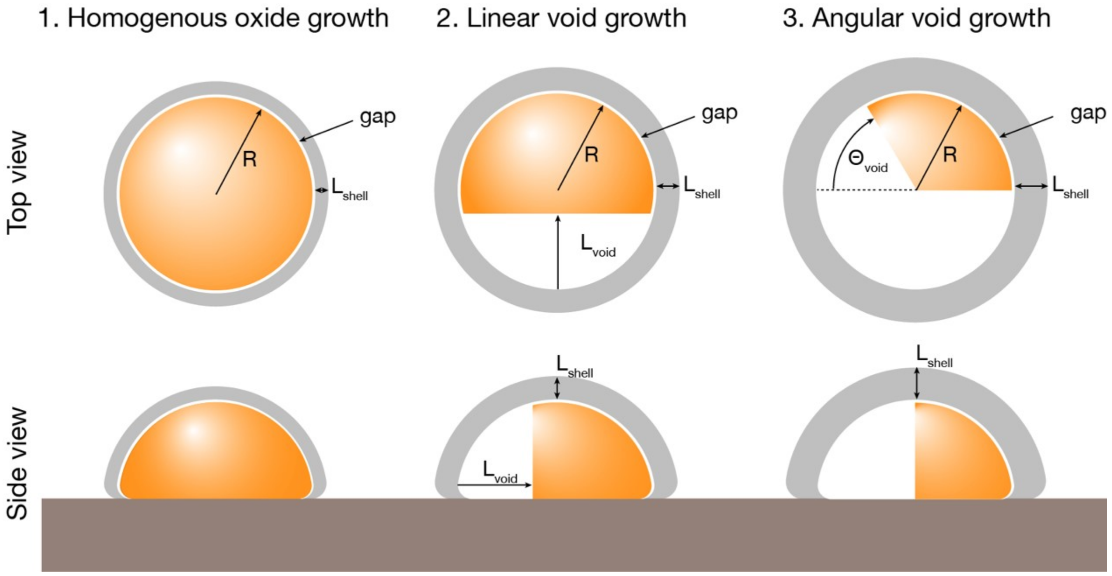

Figure S4.7: The model for NK void nucleation and growth. *Top and side views of the stages of oxidation following the homogeneous oxide growth modelled by FDTD simulations. The different layers are all drawn to scale: 1. Homogeneous oxide growth:* δ *= 15 – 20 % volume oxidation, 2. linear void growth:* δ *= 25 – 60 % oxidation, and 3. angular void growth:* δ *= 65 – 95 % oxidation.*

Table S4.3: *Parameters used in the FDTD simulations.*

2^{nd} phase: Linear void growth		
Volume oxidation δ (%)	**L_{shell} (nm)**	**L_{void} (nm)**
25	4.5	7.8
30	5.3	13.2
35	6.0	17.2
40	6.8	20.7
45	7.5	23.9
50	8.1	26.9
55	8.8	29.8
60	9.4	32.6
3^{rd} phase: Angular void growth		
Volume oxidation δ (%)	**L_{shell} (nm)**	**Θ_{void} (°)**
65	10.1	19.6
70	10.7	42.5
75	11.3	65.4
80	11.8	88.3
85	12.4	111
90	12.9	134
95	13.5	157

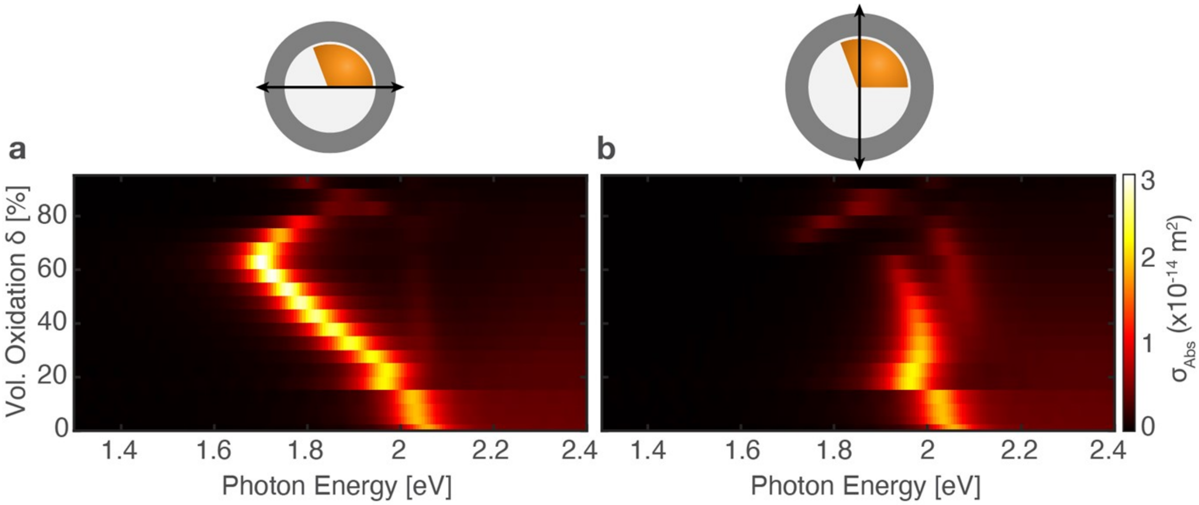

Figure S4.8: Polarization dependent LSPR evolution. *The simulated absorption cross-section as function of volume oxidation,* δ*, using the FDTD model summarized in Figure S4.7 and Table S4.3. The polarization of the applied electric field is indicated in the schematics above each panel.*

S4.4. The effect of the inner oxide shell growth on the LSPR

Here, the effect of on the LSPR of the inner oxide shell is explored since it is not included in the main model presented in Figure 2 and 3 in the main text. The simulated model has a constant total oxide volume and increasing ratio between the inner and outer oxide shell thicknesses, L_{in}/L_{out}, on a Cu hemisphere with $R = 35$ nm (**Fig. S4.9)**. The outer shell is simulated as porous by diluting the dielectric function of Cu_2O by 50 % with vacuum using the Maxwell-Garnett approach, while still keeping the total oxide volume constant, i.e. compensating by increasing the shell thickness. This is because of how the two different shells are growing, with the outer shell not being constrained geometrically or by the Cu lattice, and is therefore always polycrystalline. The 50 % dilution is an estimated upper limit for the porosity in the outer oxide which will result in a larger effect when increasing the ratio L_{in}/L_{out} in **Fig. S4.9**, hence, this is a maximum estimation of the effect of the inner oxide shell on the LSPR.

Increasing the inner-to-outer-oxide-shell ratio, L_{in}/L_{out}, leads to a slight red-shift and increasing absorption cross-section. This can be understood as the effective refractive index closest to the Cu metal interface is increased, when the L_{in}/L_{out} increases, which gives a red-shift. The choice to omit the inner shell from the FDTD model yields a slightly larger error at the higher temperatures for which the inner oxide shell is thicker but it does not change the overall response and conclusions, therefore we choose to omit it for simplicity in the model.

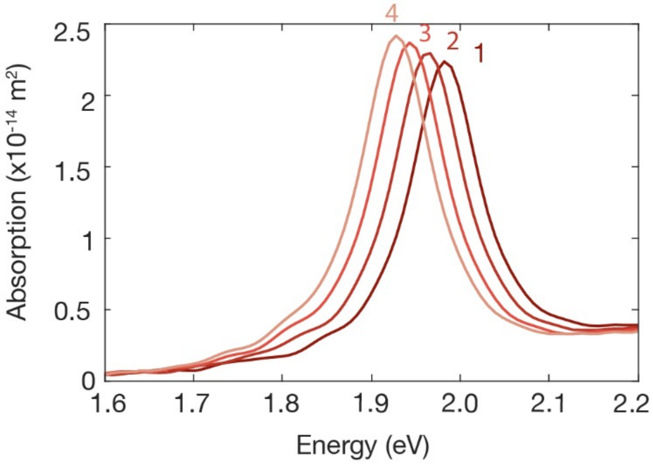

Figure S4.9: *Simulated absorption cross-sections of a Cu hemisphere (R = 35 nm) at 30 % oxidation fraction (void omitted in this example) with increasing inner-to-outer-oxide-shell ratio,* L_{in}/L_{out}. *The inner shell* (Cu_2O) *and outer shell (50 % diluted* Cu_2O) *are separated by a 1 nm vacancy gap layer. The shell thicknesses for each of the spectra are; (1)* $L_{in} = 0$ *nm,* $L_{out} = 10.2$ *nm, (2)* $L_{in} = 1$ *nm,* $L_{out} = 8.2$ *nm, (3)* $L_{in} = 2$ *nm,* $L_{out} = 6.2$ *nm and (4)* $L_{in} = 3$ *nm,* $L_{out} = 4.2$ *nm.*

S5. Fitting multiple oxidation models to the experimental data

In this section, we discuss the fitting of oxide growth kinetics in terms of the traditional Cabrera-Mott equation for thin oxide films and the general Johnson-Mehl-Avrami-Kolmogorov nucleation model.

S5.1. Cabrera-Mott kinetics

For all 7 particles studied at 50 °C, oxide growth was limited to an average oxide thickness of 5.5 ± 0.7 nm after 90 minutes O_2 exposure. The transition from the oxide island nucleation to a homogenous shell was observed from the ADF STEM images to take place after 10 minutes of O_2 exposure at 50 °C. To this end, the Cabrera-Mott[4] (CM) model for self-limited oxide thin film growth was fitted to the oxide thickness, L, of the 7 particles oxidized at 50 °C after the initial nucleation phase (**Fig. S5.1**). In the CM model, the oxide growth is governed by the potential induced by electrons tunneling from the metal to oxide surface, producing a static electric field that drives the diffusion of cations across the oxide. The tunneling rate decreases exponentially as the oxide grows thicker. We have chosen to apply the CM model from the point in time where a homogenous oxide shell is observed in the STEM images at 10 minutes, i.e. when the initially formed oxide islands have coalesced.

The oxide growth rate according to the CM model is described by Eq. S1[4,5]

$$\frac{dL}{dt} = \Omega_{ox} n \nu e^{-\frac{W}{k_B T}} e^{\frac{\frac{1}{2}qaE}{k_B T}} \tag{S1}$$

where Ω_{ox} is the volume increase per metal ion, n is the number of ions in defect positions per unit area, ν is the attempt frequency for ion jumping, q is the valence charge of the ion, a is the distance of the ion jump, k_B is the Boltzmann constant and T is the temperature. The static electric field $E = -\frac{\phi_{Mott}}{L} = \frac{(\epsilon + W_{ads} - \phi_0)}{eL}$, where ϵ is the electron affinity of O, E_{ads} is the adsorption energy of O^-, ϕ_0 is the metal work function and e is the elementary charge. The barrier for the ion jump has two contributions $W = W_i + U$, where W_i is the barrier to extract the ion from the metal lattice and U is the barrier for diffusion from one site in the oxide lattice to the next.

The differential equation S1 was solved numerically in Matlab (*ode45*) and fitted to the experimental data by optimizing the parameters ϕ_{Mott} and W. The values used for the other parameters are presented in **Table S5.1**. The average value obtained for the Mott potential ϕ_{Mott} = -3.5 ± 1 V is within a reasonable range when estimating the energies $\phi_{Mott} = (\epsilon + E_{ads} - \phi_0)/e$, ϵ = 1.46 eV,[6] $E_{ads} <$ 1 eV[7] and 4.5 $< \phi_0 <$ 5 eV,[8–10] which yields ϕ_{Mott} about -2 to -3 eV. The barrier W = 1.1 ± 0.05 eV is in reasonable agreement with corresponding literature[4,11].

Table S5.1: *The values used in the fit to the CM model.*

Parameter	Value
Ω_{ox}	0.0199 nm^3
$\boldsymbol{n}$	8
ν	10^{12} s^{-1}
q	$1e$
a	0.43 nm
T	323 K

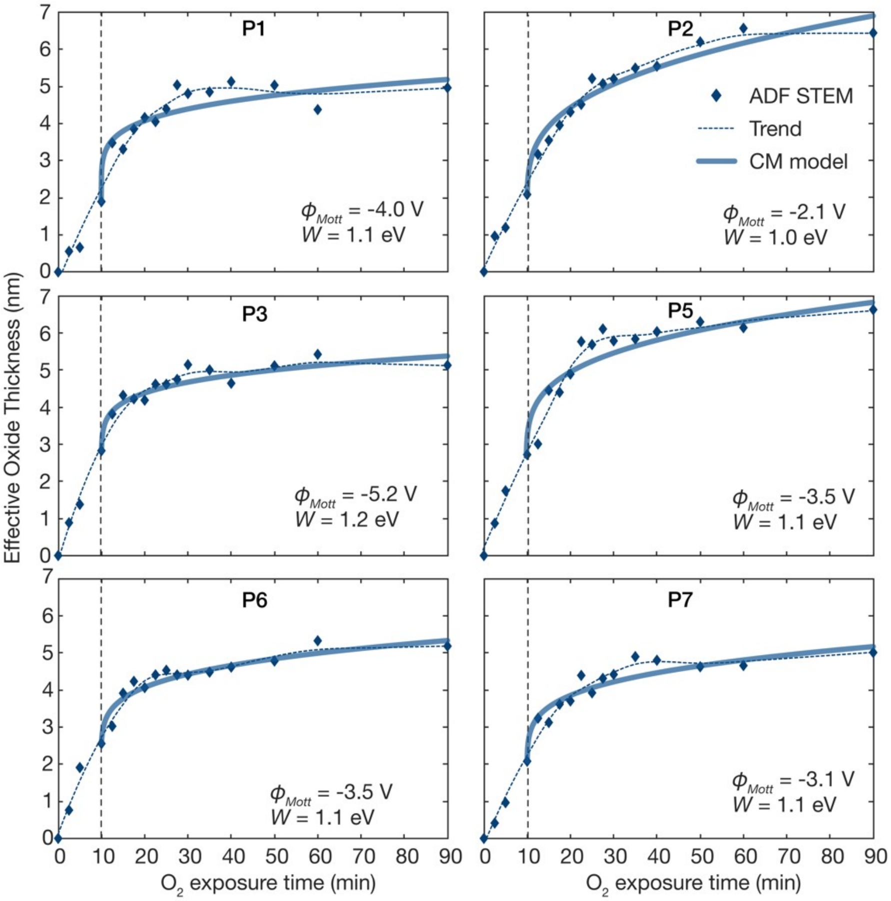

Figure S5.1: Self-limited oxide growth according to the CM model. *The effective oxide shell thickness measured from ADF STEM images of 6 additional particles oxidized at 50 °C (cf. Figure. S2.1). The oxide thickness is fitted to the CM equation, starting when the oxide islands have coalesced into a homogeneous oxide shell, i.e., after 10 minutes. The Mott potential,* ϕ_{Mott}*, and the barrier, W, for cation extraction and diffusion across the oxide is indicated for each particle, the average of all 7 particles oxidized at 50 °C are* $\bar{\phi}_{Mott}$ *= -3.5 ± 1 V and* $\bar{W}$ *= 1.1 ± 0.05 eV.*

S5.2. Johnson-Mehl-Avrami-Kolmogorov nucleation kinetics

Below, the data are fitted to the general Johnson-Mehl-Avrami-Kolmogorov (JMAK) nucleation model[12–14] for isothermal reactions, which is described as

$$X(t) = 1 - e^{-(kt)^n} \tag{S2}$$

where X is the amount of transformed material, which in our case is the amount of metal transformed to oxide, $k(T)$ is a temperature dependent rate constant often expressed by an Arrhenius equation, and n is the Avrami exponent, which is usually an integer or half-integer.

The model can describe the initial oxide island nucleation, but has to be scaled to define some state that corresponds to $X = 1$, which is the point when the transformation is complete. Two possible choices could be considered; i) when the surface is completely covered by oxide, or ii) when the complete metal volume is transformed. The first option would make sense for describing the oxide nucleation on the surface similarly to Ref. [15]. However, the number of data points in this region is limited to four. The second option of using the full volume oxidation as $X = 1$, i.e. $X = \delta$, can well describe the particles where δ equal/close to 100 % is reached. The second option gives rate constants, k, that are comparable between the particles, which we make use of in the Arrhenius analysis in Figure 6b in the main text. However, this approach does not capture the limiting thickness at 50 °C and cannot be applied to the full data set.

The JMAK model applied to the volume oxidation fractions (i.e. $X = \delta$) for the higher temperatures, is presented in **Figure S5.2**. These fits give reasonable values of the Avrami exponent n ranging from 1 to 2. Generally, the Avrami exponent can be expressed as $n = N_d g + B$,[14] where N_d is the dimensionality of the nucleation, g is a parameter that depends on the growth rate ($g = 1$ for linear growth, $g = 0.5$ for parabolic growth rate i.e. diffusion limited), moreover $B = 0$ for site saturated nucleation and $B = 1$ if new sites for transformation nucleate. In our case, the nucleation is surface limited and initially new nucleation sites are formed. Therefore, we can estimate the parameters as $N_d = 2$ and $B = 1$, which for the fit at $T = 200$ °C ($n \approx 2$) results in $g = 0.5$, meaning we are in the diffusion limited regime. For lower temperatures, we find $n \approx 1.5$, which means g and/or B must have a lower value compared to those at 200 °C.

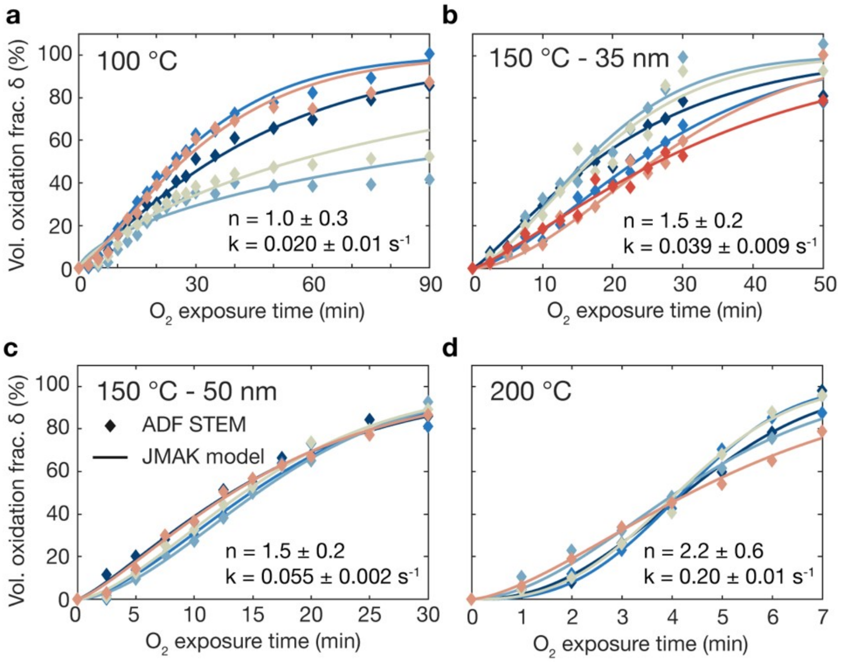

Figure S5.2: The JMAK nucleation model to the volume oxidation fraction. *The JMAK fit to the experimental data of each particle oxidized at (a) 100 °C (R_0 = 35 nm), (b) 150 °C with R_0 = 35 nm, (c) 150 °C with R_0 = 50 nm, and (d) 200 °C (R_0 = 35 nm). The mean Avrami exponent, n, and the rate constant, k, are indicated for each temperature. The mean RMSE of the fits at each temperature are all between 0.02 – 0.05. One of the particles in (a, b, d) are included in Figure 6a in the main text.*

S5.3. Arrhenius analysis

The rate constants obtained from the JMAK fit to the volume oxidation fractions δ (cf. **Fig. S5.2**), depend on temperature and can as such be described by an Arrhenius equation $k(t) = k_0 e^{\frac{-E_a}{k_B T}}$, by means of which an apparent activation energy can be extracted by fitting to $\log(k) = \log(k_0) - \frac{E_a}{k_B T}$ (**Fig. S5.3**). The apparent activation energy obtained from the JMAK fit to δ in **Figure S5.2** is 0.37 ± 0.1 eV, which is in the lower range of previously reported values[16–18].

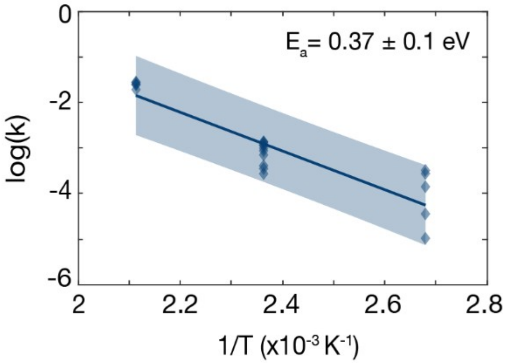

Figure S5.3: Arrhenius analysis based on the JMAK rate constant. *The Arrhenius plot of the logarithm of the rate constant vs. the inverse temperature. The rate constant, k, was obtained by fitting the JMAK model to the volume oxidation fraction, δ, in Figure S5.2. The data are the same as in Figure 6b in the main text.*

An apparent activation energy can also be extracted without assuming any particular kinetic model, but instead by looking at a characteristic time, τ, to reach a specific volume oxidation fraction, δ. Based on the δ extracted from STEM images (**Fig. S5.4**) the characteristic times to reach $\delta = 20$ and 50 %, τ_{20} and τ_{50}, are calculated by interpolating the experimental data (gray line). Equivalent to above, the typical Arrhenius analysis yields the apparent activation energies from the fit to $\log(\tau) = \log(\tau_0) - \frac{E_a}{k_B T}$ (**Fig. S5.5**). The numbers obtained from both this analysis and the one above can only be thought of as qualitative due to the small data set of three temperatures.

However, the obtained $E_a = 0.36 \pm 0.1$ eV compares well with that obtained from the JMAK fit and is within the range reported in the literature[16–18].

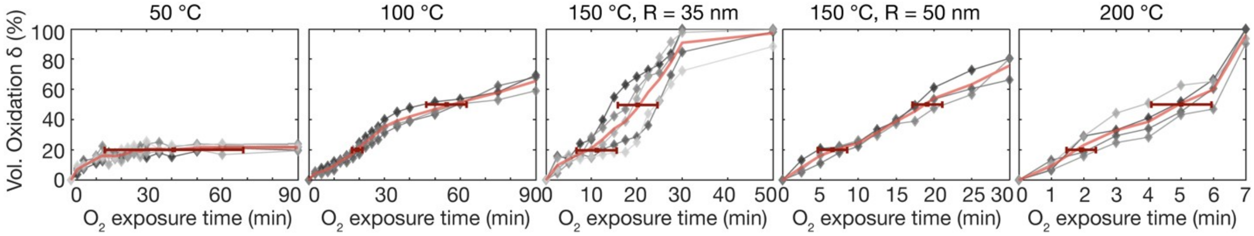

Figure S5.4: Extracting the characteristic times, τ_{20} **and** τ_{50}***, by interpolation.*** *The oxidation volume fractions, δ, at 50, 100, 150 and 200 °C as function of* O_2 *exposure time. The δ-values (gray 🕘) extracted for each particle from each ADF STEM frame during oxidation. The experimental data points are linearly interpolated (pink line, only the average is shown) to obtain the characteristic times to reach 20 and 50 % oxidation (red). The error bars are the standard deviation of the characteristic time from 3-7 particles to reach the 20 and 50 % volume oxidation.*

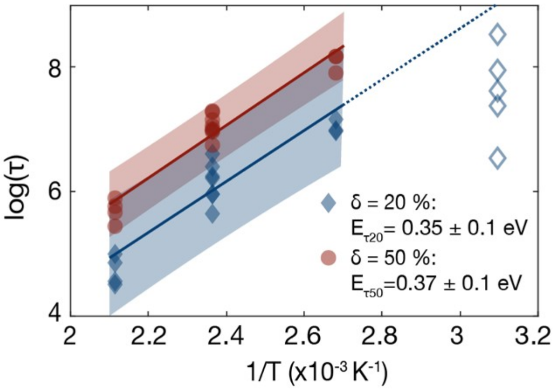

Figure S5.5: Arrhenius plots of the characteristic times. *The times to reach 20 %,* τ_{20}*, (blue 🕘) and 50 %,* τ_{50}*, (red ●) for 100, 150 and 200 °C. The fits to the Arrhenius equation are the solid lines and the shaded areas show the 95 % confidence interval of the fits. The data plotted as unfilled markers (✵) are obtained from the oxidation at 50 °C and are excluded from the fit. The extrapolation of the line (dashed) shows that the 50 °C data are not matching the fit. The apparent activation energies are* $E_{\tau_{20}} = 0.35 \pm 0.1$ *eV and* $E_{\tau_{50}} = 0.37 \pm 0.1$ *eV.*

Additionally, the effective outer and inner oxide shell thickness (calculated as a homogeneous oxide thickness from the inner/outer oxide area and particle radius measured in STEM images) are analyzed in a similar qualitative Arrhenius analysis to extract approximate apparent activation energies. As above, the numbers can only be thought of as qualitative due to the limited temperature data set. However, the results still point in the same direction as the oxide thickness growth over time (Figure 5 in the main text), i.e., that the oxide growth rate increases with temperature and the outer oxide grows faster at all temperatures. The times to reach 2 and 5 nm for the outer and 0.5 nm for the inner oxide shells, are extracted by interpolating (gray line) the oxide thickness extracted from STEM images (🕐 in **Fig. S5.6-5.7**) and finding the characteristic times, τ. The chosen thicknesses have data for at least three temperatures. The corresponding Arrhenius plots (**Fig. S5.8**) yield an average $E_{\text{out}} = 0.29 \pm 0.1$ eV for the outer shell and $E_{\text{in}} = 0.45 \pm 0.1$ eV for the inner shell. This indicates about 50 % higher activation energy for the inner shell compared to the outer shell.

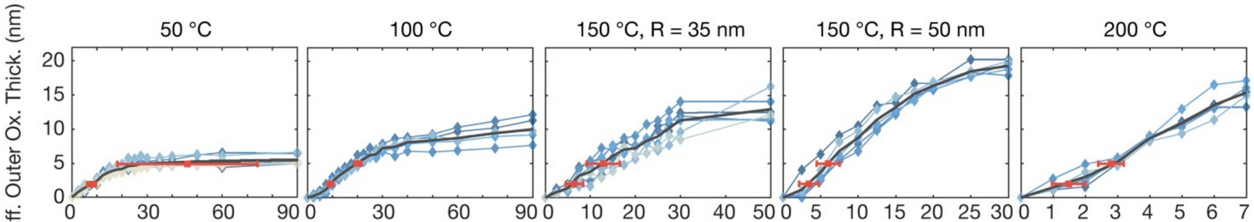

Figure S5.6: Extracting the characteristic times to reach 2 or 5 nm outer oxide. *The effective oxide shell thicknesses (blue 🕐) extracted for each particle in each STEM frame during oxidation. The experimental data points are linearly interpolated (gray line, only the average is included) to obtain the characteristic times to reach 2 and 5 nm oxide thickness (red). The error bars are the standard deviation of the characteristic times from 5-7 particles to reach 2 and 5 nm oxide thickness, respectively.*

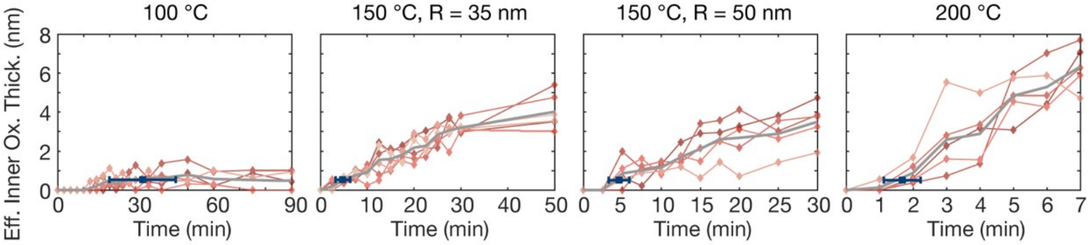

Figure S5.7: Extracting the characteristic times to reach 0.5 nm inner oxide. *The effective inner oxide shell thickness (red 🕐) for each particle from each frame during oxidation. The experimental data points are linearly interpolated (gray line, only the average is included) to obtain the* *characteristic times to reach 0.5 nm oxide thickness (blue). The error bars are the standard deviation of the characteristic times from 5-7 particles to reach 0.5 nm inner oxide thickness.*

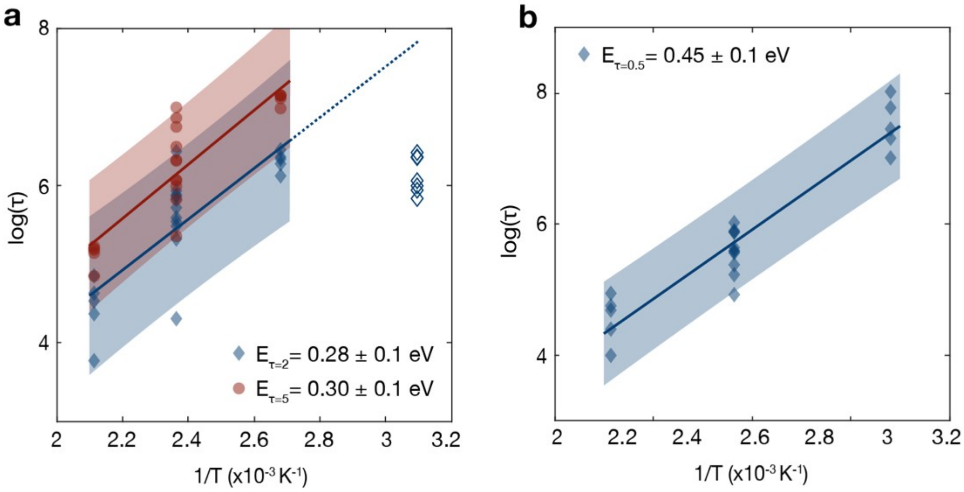

Figure S5.8: Arrhenius plots of the inner and outer oxide shells. *The logarithm of the times of (a) the outer oxide thickness to reach 2 (blue ◷) and 5 nm (red ●) and (b) the inner oxide shell to reach 0.5 nm (◷), vs. the inverse temperature. The solid lines are the Arrhenius fit to the particles oxidized at 100, 150 and 200 °C and the shaded areas show the 95 % confidence interval of each fit. Only the data from 100, 150 and 200 °C are used for the fitting (50 °C data marked by unfilled ✵). Some of the data (the inner shell and the 5 nm fit for the outer shell) are the same as in Figure 6c and d in the main text.*

References

1. Ngantcha, J. P., Gerland, M., Kihn, Y. & Riviere, A. Correlation between microstructure and mechanical spectroscopy of a Cu-Cu2O alloy between 290K and 873K. *Eur. Phys. J. Appl. Phys.* **29**, 83–89 (2005).
2. Wang, Y. *et al.* Electronic structures of Cu2O, Cu4O3, and CuO: A joint experimental and theoretical study. *Phys. Rev. B* **94**, (2016).
3. Mattsson, A., Panas, I., Siegbahn, P., Wahlgren, U. & Akeby, H. Model studies of the chemisorption of hydrogen and oxygen on Cu(100). *Phys. Rev. B* **36**, 7389 (1987).
4. Cabrera, N. & Mott, N. F. Theory of the oxidation of metals. *Rep. Prog. Phys.* **12**, (1949).
5. Ermoline, A. & Dreizin, E. L. Equations for the Cabrera-Mott kinetics of oxidation for spherical nanoparticles. *Chem. Phys. Lett.* **505**, 47–50 (2011).
6. Chaibi, W., Peláez, R. J., Blondel, C., Drag, C. & Delsart, C. Effect of a magnetic field in photodetachment microscopy. *Eur. Phys. J. D 2010 581* **58**, 29–37 (2010).
7. Lian, X., Xiao, P., Yang, S. C., Liu, R. & Henkelman, G. Calculations of oxide formation on low-index Cu surfaces. *J. Chem. Phys.* **145**, 44711 (2016).
8. Anderson, P. A. The work function of copper. *Phys. Rev.* **76**, 388–390 (1949).
9. Singh, B. & Mehta, B. R. Relationship between nature of metal-oxide contacts and resistive switching properties of copper oxide thin film based devices. *Thin Solid Films* **569**, 35–43 (2014).
10. Greiner, M. T., Chai, L., Helander, M. G., Tang, W. M. & Lu, Z. H. Transition metal oxide work functions: The influence of cation oxidation state and oxygen vacancies. *Adv. Funct. Mater.* **22**, 4557–4568 (2012).
11. Karimi, M., Tomkowski, T., Vidali, G. & Biham, O. Diffusion of Cu on Cu surfaces. *Phys. Rev. B* **52**, 5364 (1995).
12. Fanfoni, M. & Tomellini, M. The Johnson-Mehl-Avrami-Kolmogorov model: A brief review. *Nuovo Cim. della Soc. Ital. di Fis. D - Condens. Matter, At. Mol. Chem. Physics, Biophys.* **20**, 1171–1182 (1998).
13. Yang, J. C., Evan, D. & Tropia, L. From nucleation to coalescence of Cu2O islands during in situ oxidation of Cu(001). *Appl. Phys. Lett.* **81**, 241–243 (2002).
14. Starink, M. J. On the meaning of the impingement parameter in kinetic equations for nucleation and growth reactions. *J. Mater. Sci. 2001 3618* **36**, 4433–4441 (2001).
15. Auge, A., Weddemann, A., Vogel, B., Wittbracht, F. & Hütten, A. A level set based approach for modeling oxidation processes of ligand stabilized metallic nanoparticles. (2010).

16. Albinsson, D., Nilsson, S., Antosiewicz, T. J., Zhdanov, V. P. & Langhammer, C. Heterodimers for in situ plasmonic spectroscopy: Cu nanoparticle oxidation kinetics, Kirkendall effect, and compensation in the arrhenius parameters. *J. Phys. Chem. C* **123**, 6284–6293 (2019).

17. Susman, M. D., Feldman, Y., Bendikov, T. A., Vaskevich, A. & Rubinstein, I. Real-time plasmon spectroscopy study of the solid-state oxidation and Kirkendall void formation in copper nanoparticles. *Nanoscale* **9**, 12573–12589 (2017).

18. Rice, K. P., Paterson, A. S. & Stoykovich, M. P. Nanoscale Kirkendall effect and oxidation kinetics in copper nanocrystals characterized by real-time, in situ optical spectroscopy. *Part. Part. Syst. Charact.* **32**, 373–380 (2015).